

# An ab initio study of the band gap of high-entropy silicides based on $\text{FeSi}_2$

Jørn-Marcus Høylo-Rosenberg



Thesis submitted for the degree of  
Master in Materials Science for Energy and  
Nanotechnology  
60 credits

Department of Chemistry  
Faculty of mathematics and natural sciences

UNIVERSITY OF OSLO

Spring 2022



**An ab initio study of the band  
gap of high-entropy silicides  
based on FeSi<sub>2</sub>**

Jørn-Marcus Høylo-Rosenberg

© 2022 Jørn-Marcus Høylo-Rosenberg

An ab initio study of the band gap of high-entropy silicides based on  $\text{FeSi}_2$

<http://www.duo.uio.no/>

Printed: Reprosentralen, University of Oslo

# **Abstract**

# Contents

<b>1</b>	<b>Introduction</b>	<b>1</b>
<b>I</b>	<b>Theory</b>	<b>3</b>
<b>2</b>	<b>High-Entropy alloys</b>	<b>4</b>
2.1	Fundamentals . . . . .	4
2.2	Core effects and properties . . . . .	7
<b>3</b>	<b>Modeling of random alloys</b>	<b>9</b>
3.1	The Special Quasi-random Structure model . . . . .	9
3.1.1	Mathematical description . . . . .	10
3.1.2	Applications to high-entropy alloys . . . . .	12
<b>4</b>	<b>Density Functional Theory</b>	<b>16</b>
4.1	Review of Quantum Mechanics . . . . .	17
4.1.1	The Shrödinger equation . . . . .	17
4.1.2	Approximations to the many-body Shrödinger equation . . . . .	18
4.2	Kohn-Sham density functional theory . . . . .	20
4.2.1	Density functional theory . . . . .	20
4.2.2	The Kohn-Sham Equation . . . . .	21
4.3	Limitations of DFT . . . . .	22
<b>II</b>	<b>Method</b>	<b>24</b>
<b>5</b>	<b>Practical aspects of DFT</b>	<b>25</b>
5.1	The Exchange-Correlation functional . . . . .	25
5.1.1	Local density approximation . . . . .	26
5.1.2	Generalized gradient approximation . . . . .	26
5.1.3	Meta-GGA . . . . .	26
5.1.4	Hybrid functionals . . . . .	27
5.1.5	Outlook . . . . .	28
5.2	Plane waves and reciprocal space . . . . .	28
5.3	Self-consistent field calculation . . . . .	31

<b>6</b>	<b>Computational details</b>	<b>32</b>
6.1	Settings and dependencies . . . . .	32
6.2	Material . . . . .	33
<b>III</b>	<b>Results and Discussion</b>	<b>35</b>
<b>7</b>	<b>The high-entropy silicide (CrFeMnNi)Si<sub>2</sub></b>	<b>36</b>
7.1	$\beta$ -FeSi <sub>2</sub> . . . . .	36
7.2	(CrFeMnNi)Si <sub>2</sub> . . . . .	37
7.2.1	The band gap . . . . .	39
7.2.2	Local and projected density of states . . . . .	43
7.2.3	The band gap with SCAN and HSE06 . . . . .	45
7.2.4	Pair distribution functions . . . . .	50
7.2.5	Charge density . . . . .	51
7.2.6	SQS size . . . . .	52
<b>8</b>	<b>Alternative compositions</b>	<b>56</b>
8.1	Exploring the quaternary phase diagram . . . . .	56
8.2	High entropy silicides with cobalt/titanium . . . . .	60
8.3	Negative systems . . . . .	64
<b>IV</b>	<b>Conclusion and future work</b>	<b>65</b>
<b>9</b>	<b>Conclusion</b>	<b>66</b>
<b>10</b>	<b>Future work</b>	<b>68</b>
<b>A</b>	<b>Figures</b>	<b>69</b>
A.1	Density of states . . . . .	69
A.2	Projected density of states . . . . .	71
A.3	Charge density . . . . .	72
A.4	Other . . . . .	73

# List of Figures

2.1	Formation of HEA based on $\delta$ and $N$ . Figures adopted from [hea2016_ch2] . . . . .	6
2.2	A schematic illustration of lattice distortion in high-entropy alloys. Figure from [owen_jones_2018] . . . . .	8
3.1	PDFs of (a) 20 and (b) 250 atom SQS models of CrFeMnNi [hea2016_ch10] . . . . .	13
3.2	Density of states with SQS and MC/MD of FCC CoCrFeNi, figure from [hea2016_ch10] . . . . .	14
3.3	Probability distribution functions with SQS and MC/MD of HCP CoOsReRu [hea2016_ch10] . . . . .	14
4.1	Number of DFT studies per year from 1980 to 2021 [dimensions]. . . . .	16
5.1	Jacob's ladder [jacob]. . . . .	25
5.2	Calculated to experimental band gap measurements of Becke-Johnson, modified Becke-Johnson and SCAN functionals [xc_benchmark] . . . . .	27
5.3	Self consistent iterations of a DFT calculation. Figure adopted from the lecture notes in FYS-MENA4111 [persson2020] . . . . .	31
6.1	Five distinct 48-atom SQSs of $\text{Cr}_4\text{Fe}_4\text{Mn}_4\text{Ni}_4\text{Si}_{32}$ based on the $\beta$ -FeSi <sub>2</sub> crystal structure. Manganese atoms are represented as purple spheres, chromium as dark blue and silicon as light blue, followed by iron and nickel presented as gold and silver spheres respectively. The respective SQSs are denoted as A, B, C, D and E. Figures illustrated with VESTA [vesta] . . . . .	34
7.1	Density of states [states/eV] of $\beta$ -FeSi <sub>2</sub> . . . . .	37
7.2	Density of states [states/eV] of SQS D of (CrFeMnNi)Si <sub>2</sub> . . . . .	39
7.3	Density of states [states/eV] of SQS B of (CrFeMnNi)Si <sub>2</sub> . . . . .	39
7.4	Local density of states [states/eV] of Si (SQS D). . . . .	43
7.5	Local density of states [states/eV] of (a) Cr, (b) Mn, (c) Fe, (d) Ni in SQS D. . . . .	43
7.6	Projected density of states [states/eV] of SQS D. . . . .	44
7.7	Projected density of states [states/eV] of SQS D and B around $E_F$ . . . . .	44



7.8	Density of states [states/eV] illustrating the band gaps of SQS E and D with PBE and SCAN. . . . .	46
7.9	Density of states [states/eV] of SQS B with HSE06. . . . .	46
7.10	Pair distribution functions of SQS D (top) and B (bottom) . .	50
7.11	Charge density in SQS A, B, D and E of $\text{Cr}_4\text{Fe}_4\text{Mn}_4\text{Ni}_4\text{Si}_{32}$ . .	51
7.12	CPU time of 48, 96 and 192-atom SQSs of $(\text{CrFeMnNi})\text{Si}_2$ . .	52
7.13	Density of states of SQS E 192 atom SQS. . . . .	54
7.14	Pair distribution functions of $(\text{CrFeMnNi})\text{Si}_2$ (top) 48-atom SQS, (middle) 96-atom SQS, (bottom) 192-atom SQS. . . . .	55
8.1	Projected density of states of (a) $\text{Cr}_3\text{Fe}_3\text{Mn}_7\text{Ni}_3\text{Si}_{32}$ (SQS B), (b) $\text{Cr}_5\text{Fe}_5\text{Mn}_3\text{Ni}_3\text{Si}_{32}$ (SQS C), (c) $\text{Cr}_5\text{Fe}_3\text{Mn}_5\text{Ni}_3\text{Si}_{32}$ (SQS A), (d) $\text{Cr}_3\text{Fe}_5\text{Mn}_5\text{Ni}_3\text{Si}_{32}$ (SQS D) . . . . .	58
8.2	Projected density of states of $\text{Cr}_3\text{Fe}_3\text{Mn}_3\text{Ni}_7\text{Si}_{32}$ around $E_F$ .	59
8.3	Projected density of states of $(\text{CrFeMnCo})\text{Si}_2$ . . . . .	63
8.4	Projected density of states . . . . .	63
8.5	Density of states of SQS A and E of $(\text{CoFeMnNi})\text{Si}_2$ . . . . .	64
A.1	Density of states SQS A $(\text{CrFeMnNi})\text{Si}_2$ with PBE. . . . .	69
A.2	Density of states SQS E $(\text{CrFeMnNi})\text{Si}_2$ with PBE. . . . .	70
A.3	Density of states SQS C $(\text{CrFeMnNi})\text{Si}_2$ with PBE. Nedos represent the number of points in the DOS calculation. . . .	70
A.4	Projected density of states SQS A . . . . .	71
A.5	Projected density of states SQS B . . . . .	71
A.6	Projected density of states SQS E . . . . .	72
A.7	Charge density of SQS C. . . . .	72
A.8	Density of states SQS C $\text{Cr}_5\text{Fe}_5\text{Mn}_3\text{Ni}_3\text{Si}_{32}$ , illustrating the small finite DOS at $E_F$ due to the impurity gap. . . . .	73

# List of Tables

7.1	Total energy, magnetic moment, band gap and formation energy of 5 SQS of (CrFeMnNi)Si <sub>2</sub> . . . . .	37
7.2	Band gap of five SQSs of (CrFeMnNi)Si <sub>2</sub> in spin up, down and total, calculated from the Kohn-Sham eigenvalues. . . .	40
7.3	Band gap of SQS D as a function of occupancy cutoff in the eigenvalues. . . . .	41
7.4	Band gap of five supercells of (CrFeMnNi)Si <sub>2</sub> calculated with PBE, SCAN and HSE06. . . . .	45
7.5	Minimum gap between k-point in valence band and conduction band in SQS B from PBE, SCAN and HSE06 . . . . .	47
7.6	Band gap from HSE06 calculations with Gaussian smearing, with smearing width $\sigma$ equal to 0.05 eV and 0.005 eV, and the tetrahedron method (TBC). "-" means that the band gap is unchanged between occ = 0.5 and occ = 0.01. . . . .	48
7.7	Total energy, magnetic moment and formation energy of 48, 96 and 192 atom SQSs of (CrFeMnNi)Si <sub>2</sub> . . . . .	53
7.8	Band gap of SQSs of 48, 96 and 192-atoms of (CrFeMnNi)Si <sub>2</sub> . The names are arbitrary, ie A in 48 does not equal A in 96 or A in 192. The values listed in <i>cursive</i> indicate a defect band gap. . . . .	53
8.1	Summary composition diagram . . . . .	56
8.2	Band gaps of various compositions of (CrFeMnNi)Si <sub>2</sub> . Most stable SQS of a set is highlighted in bold text, defect/impurity band gap are listed in cursive. Some SQSs were excluded from the table due to unsuccessful calculations. . . . .	57
8.3	Overview new compositions . . . . .	60
8.4	Final magnetic moment of the utmost stable SQS of each composition. . . . .	61
8.5	The band gap in spin up/down and total of the most stable SQS of high-entropy silicides based on $\beta$ -FeSi <sub>2</sub> with cobalt/titanium. . . . .	62

# Acknowledgments

I would like to express my gratitude towards my supervisor Ole Martin Løvvik. For always being available and prioritize my work from the first day to the last. Coming into this project, I had no prior knowledge of density functional theory or quantum mechanical modeling. So, for your guidance in this project I am truly thankful, and know that this project would have been impossible without you. I also feel as if I have made a friend and someone I could talk through throughout this project. Due to the oddity of these recent years with the covid-19 outbreak and self-isolation this have been very important to my sanity and mental health combined with the difficulty involved in writing a master theses. On this same note, I would like to thank all my friends and family members that have been there and believed in me, and always reminding me to stay positive.

# Chapter 1

## Introduction

A major concern in the energy sector is the loss of energy as waste heat. An example of this is seen in for instance [1], where they estimated that about 60 percent of the energy produced in USA in 2012 was lost as waste heat. Contrary to most energy sources that suffer from this problem of losing energy to heat, thermoelectricity can generate electricity from heat by what's known as the Seebeck effect [2]. Thus, thermoelectricity have many promising applications, for example one could imagine a conjunction between thermoelectric generators and mechanical generators to recover a portion of the waste heat produced by the latter. However, currently thermoelectricity is of limited practical use due to a lack of efficient thermoelectric materials. This can be explained from the thermoelectric figure of merit, composed by the Seebeck Coefficient  $S$ , electrical conductivity  $\sigma$ , temperature  $T$  and the thermal conductivity, in the following relation [3]

$$zT = \frac{S^2 \sigma T}{\kappa}. \quad (1.1)$$

Thus, an efficient thermoelectric material consist of three dependent factors: A high Seebeck coefficient, high electrical conductivity, and low thermal conductivity. A popular strategy to achieve this relation is the phonon-glass electron crystal approach [4], in which one will introduce complexity and anharmonicity to the crystal lattice by some means to increase levels of phonon scattering, without also increasing the scattering of electrons. Furthermore good thermoelectrics are narrow gap semiconductors, as explained in [5], that found the highest  $zT$  values for semiconductors with a band gap between  $6-10 k_B T$ , which at room temperature equals around 0.2 eV.

In this project we will look at high-entropy alloys as potential thermoelectric materials. High-entropy alloys are a novel material class that extends the concept of traditional binary-alloys such as steel, to multi-component alloys. The name "high-entropy" stems from the fact that mixing a larger number of elements increase the configurational entropy of the solution, that contribute to stabilize the materials. These materials are in particular known for their strong mechanical properties [6], for instance high strength at elevated temperatures. Furthermore evidence of

low thermal conductivity originating from a disordered crystal structure. Hence, provided that we can find narrow gap high-entropy alloys, these could be relevant and promising high  $zT$  thermoelectric materials.

Specifically, in this project we will look at high-entropy silicides. These are a lesser studied subclass of high-entropy alloys. The first experimentally synthesized high-entropy silicide was found in 2019 by Gild. et al [7]. He found a first of its kind single-phase high-entropy disilicide  $(\text{MoNbTaW})\text{Si}_2$ . This silicide adopted the hexagonal C40 crystal structure, and displayed low thermal conductivity compared to conventional disilicides in the equivalent crystal structure. Additionally, very recently a master thesis student at the University of Oslo managed to synthesize three phases of non-cubic high-entropy silicides based on Si, Co, Cr, Fe, and Ni in both hexagonal and orthorhombic symmetries [8]. We base this project on silicides because firstly silicon and various transition metal-silicides are environmentally sound and silicon in particular is heavily applied in micro-electronic devices and renewable energy sources such as solar power, thus silicon based alloys could readily be implemented into these technologies. Secondly, transition metal silicides offer a good range of initial compounds with suitable band gaps for thermoelectrics [9].

This project is performed by ab initio methods in the framework of density functional theory. The disordered structure of high-entropy alloys are handled with a numerical method called special quasi-random structures. The particular materials investigated in this project will be based on the semiconductor  $\beta\text{-FeSi}_2$ . We will mainly investigate the band gap of such alloys, for this we employ three classes of functionals in DFT: GGA, meta-GGA and hybrid functionals. In addition, we will perform a brief analysis of the stability and magnetism. The potential high-entropy silicides are studied by constructing five distinct supercells of the master compound, where the iron sites are populated by a quasi-random distribution between 3d transition metals. Special emphasis are placed on alloys consisting of Cr, Fe, Mn and Ni, as these along with silicon are sustainable non-toxic elements.

We begin this project by reviewing the fundamentals and properties of high-entropy alloys, thereafter we present a theoretical description of the computational methods in this project, SQS, and DFT. Next we discuss various practical aspects of DFT such as the exchange-correlation functionals and numerical convergence, in addition to numerical settings necessary to reproduce the results in this project. Finally we present and discuss the results, which begin with the high-entropy silicide  $(\text{CrFeMnNi})\text{Si}_2$ , followed by various derivatives and alternatives to this system. In the end we give a brief conclusion of our work and discuss possible directions for future research.

# **Part I**

# **Theory**

# **Part II**

## **Method**

**Part III**

**Results and Discussion**



## Chapter 8

# Alternative compositions

Up until this point we have looked in detail at the high-entropy silicide (CrFeMnNi)Si<sub>2</sub>. In this chapter we will broaden our search of compositions based on the  $\beta$ -FeSi<sub>2</sub> structure. First, we will look at various compositions inside the quaternary phase diagram of Cr, Fe, Mn and Ni, then consider some compositions where chromium, manganese or nickel are replaced by cobalt or titanium.

### 8.1 Exploring the quaternary phase diagram

In this section, we aim to expand our search of this diagram by generating SQSs of the 48 atom model slightly away from equimolar distribution of 3d elements. The list of compositions are listed in table 8.1, with corresponding total energy, magnetic moment and formation energy in the familiar format. Ideally each composition would differ only by one element to provide a clear view of each direction in the phase diagram, but the TDEP implementation insisted in also reducing Nickel to stay consistent with the 48 atom supercell.

Composition	Toten (eV)		Mag ( $\mu_B$ )		$E_{FPA}$ (eV)
	mean	std	mean	std	mean
Cr <sub>3</sub> Fe <sub>3</sub> Mn <sub>7</sub> Ni <sub>3</sub> Si <sub>32</sub>	- 6.695	0.004	0.138	0.019	-0.300
Cr <sub>5</sub> Fe <sub>5</sub> Mn <sub>3</sub> Ni <sub>3</sub> Si <sub>32</sub>	- 6.671	0.003	0.113	0.022	-0.286
Cr <sub>5</sub> Fe <sub>3</sub> Mn <sub>5</sub> Ni <sub>3</sub> Si <sub>32</sub>	- 6.685	0.004	0.138	0.046	-0.271
Cr <sub>3</sub> Fe <sub>5</sub> Mn <sub>5</sub> Ni <sub>3</sub> Si <sub>32</sub>	- 6.680	0.004	0.094	0.021	-0.315
Cr <sub>3</sub> Fe <sub>3</sub> Mn <sub>3</sub> Ni <sub>7</sub> Si <sub>32</sub>	- 6.392	0.008	0.016	0.010	-0.285

Table 8.1: Summary composition diagram

In table 8.1 we observe that moving away from the equimolar system result in both less and more stable alloys. Clearly the most lowest formation energies (most stable) correspond to compositions rich in manganese and poor in chromium. Likewise the least stable compositions in table

8.1 contain either increased amounts of Cr or reduced amounts of Mn compared to the equimolar system. In the equimolar composition the magnetic moment was attributed to primarily Cr and Mn atoms in the lattice. In table 8.1 we observe similarly that compositions rich in Cr and Mn exhibits the largest magnetic moments and vice versa. The band gaps of the respective compositions in five unique SQSs can be seen in table 8.2 below, calculated with PBE GGA.

Composition	SQS	$E_G^{\text{up, eigen}}(0.5)$ (eV)	$E_G^{\text{dw, eigen}}(0.5)$ (eV)	$E_G^{\text{tot, eigen}}(0.5)$ (eV)
$\text{Cr}_3\text{Fe}_3\text{Mn}_7\text{Ni}_3\text{Si}_{32}$	<b>A</b>	0.339	0	0
	<b>B</b>	0.475	0	0
	C	0.134	0	0
	D	0.195	0.006	0.006
	E	0.421	0	0
$\text{Cr}_5\text{Fe}_5\text{Mn}_3\text{Ni}_3\text{Si}_{32}$	A	0.003	0	0
	<b>C</b>	0.210	0	0
	D	0.067	0.041	0.037
	E	0.362	0	0
$\text{Cr}_5\text{Fe}_3\text{Mn}_5\text{Ni}_3\text{Si}_{32}$	<b>A</b>	0.208	0	0
	B	0.405	0	0
	C	0.466	0	0
	D	0.084	0.012	0.012
	E	0.301	0	0
$\text{Cr}_3\text{Fe}_5\text{Mn}_5\text{Ni}_3\text{Si}_{32}$	A	0.392	0	0
	C	0.129	0	0
	<b>D</b>	0.260	0.100	0.100
	E	0.359	0.100	0.085
$\text{Cr}_3\text{Fe}_3\text{Mn}_3\text{Ni}_7\text{Si}_{32}$	A	0	0	0
	B	0	0	0
	C	0	0	0
	D	0	0	0
	<b>E</b>	0.040	0	0

Table 8.2: Band gaps of various compositions of  $(\text{CrFeMnNi})\text{Si}_2$ . Most stable SQS of a set is highlighted in bold text, defect/impurity band gap are listed in cursive. Some SQSs were excluded from the table due to unsuccessful calculations.

From table 8.2 we observe that most compositions are half-metals alike the equimolar system with a spin up polarization. Each composition show large variation between configurations. We note  $E_{G, \text{max}}^{\text{up}} \approx 0.5$  eV and  $E_{\text{min}}^{\text{up}} \approx 0.1$  eV in both  $\text{Cr}_3\text{Fe}_3\text{Mn}_7\text{Ni}_3\text{Si}_{32}$  and  $\text{Cr}_5\text{Fe}_3\text{Mn}_5\text{Ni}_3\text{Si}_{32}$ , and further  $E_{G, \text{max}}^{\text{up}} \approx 0.4$  eV and  $E_{\text{min}}^{\text{up}} \approx 0.1$  eV in  $\text{Cr}_3\text{FeMn}_5\text{Ni}_3\text{Si}_{32}$ . In all three of these compositions the proportion of manganese is increased relative

to the equimolar system, and two out of the three compositions contain reduced amounts of chromium. Looking at the two compositions with the least indication of a band gap  $\text{Cr}_5\text{Fe}_5\text{Mn}_3\text{Ni}_3\text{Si}_{32}$  and  $\text{Cr}_3\text{Fe}_3\text{Mn}_3\text{Ni}_7$ , these contain reduced amounts of manganese. Thus, based on the few compositions tested in this experiment we can state a relation of the band gap mainly to manganese, but also chromium.

Based on the utmost stable configuration of each composition, we observe very encouraging results in the  $\text{Cr}_3\text{Fe}_3\text{Mn}_7\text{Ni}_3\text{Si}_{32}$  composition with the largest  $E_G^{\text{up}}$  of the set of configurations, likewise the most stable SQS of the  $\text{Cr}_3\text{Fe}_5\text{Mn}_5\text{Ni}_3\text{Si}_{32}$  composition is a semiconductor with a total band gap of about 0.1 eV. In the composition  $\text{Cr}_5\text{Fe}_5\text{Mn}_3\text{Ni}_3\text{Si}_{32}$  the most stable SQS predicts a defect or impurity band gap as we discussed previously where the eigenvalues return a finite band gap despite of defect states. However we have not been able to investigate the nature and effect of this impurity band gap to further extent, likewise for the similar impurity gaps listed in table 8.2 and the 0 band gaps in spin down. Below in figures 8.1 and 8.2 we include the projected density of states around  $E_F$  of the utmost stable SQS of each composition. Because we only include and discuss the most stable SQS, the features of these figures can be subject to the uniqueness of that particular SQS rather than a distinct feature of the exact composition, but as stated previously the most stable configuration provide the most likely properties of the composition within the scope of this project.

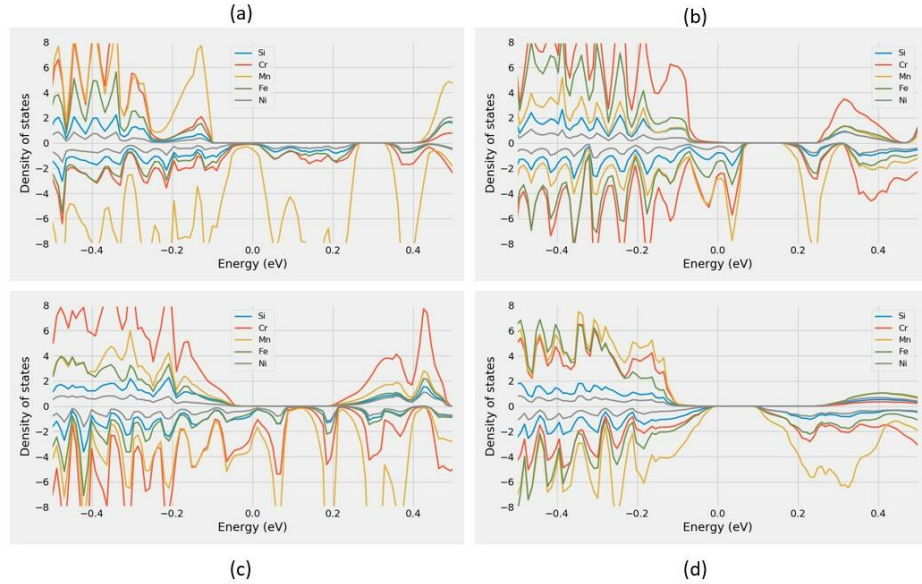


Figure 8.1: Projected density of states of (a)  $\text{Cr}_3\text{Fe}_3\text{Mn}_7\text{Ni}_3\text{Si}_{32}$  (SQS B), (b)  $\text{Cr}_5\text{Fe}_5\text{Mn}_3\text{Ni}_3\text{Si}_{32}$  (SQS C), (c)  $\text{Cr}_5\text{Fe}_3\text{Mn}_5\text{Ni}_3\text{Si}_{32}$  (SQS A), (d)  $\text{Cr}_3\text{Fe}_5\text{Mn}_5\text{Ni}_3\text{Si}_{32}$  (SQS D)

The PDOSs is in good agreement with the listed values in table 7.2.  $\text{Cr}_3\text{Fe}_3\text{Mn}_7\text{Ni}_3\text{Si}_{32}$  and  $\text{Cr}_5\text{Fe}_3\text{Mn}_5\text{Ni}_3\text{Si}_{32}$  both display sizable band gaps in

spin, while figure 8.1 d point to a total band gap around 0.1 eV for SQS D of  $\text{Cr}_3\text{Fe}_5\text{Mn}_5\text{Ni}_3\text{Si}_{32}$ . On the other hand we observe as for the 192-atom SQS a dissimilarity between the density of states band gap in  $\text{Cr}_5\text{Fe}_5\text{Mn}_3\text{Ni}_3\text{Si}_{32}$  SQS C (figure 8.1 b) and the eigenvalue (impurity) band gap listed in table 7.2. This can be better understood by figure .. in appendix .. that display a zoomed in DOS that clearly show small finite values at  $E_F$  in spin up. This DOS may resemble that of a n-doped material where the Fermi energy is pushed up in energy.

In figure 7.7 we saw that manganese distinctly occupied states in the spin down channel around  $E_F$  and was a key contributor as to why the spin down channel of  $(\text{CrFeMnNi})\text{Si}_2$  was metallic in the utmost stable SQS. This is also largely the case in the compositions shown above in figure 8.1 and 8.2, and is particularly evident in figure 8.1 where Mn dominate the spin down states around  $E_F$  in the  $\text{Cr}_3\text{Fe}_3\text{Mn}_7\text{Ni}_3\text{Si}_{32}$  composition. By reducing the number of Mn we still find that the Mn states prohibit the band gap in spin down, as seen in figure 8.1 b. In the chromium rich compositions plotted in figures 8.1 b and c, we observe that also Cr states prohibit the spin down band gap, and dominate states near  $E_F$  in spin up as well. Contrary, in the  $\text{Cr}_3\text{Fe}_3\text{Mn}_3\text{Ni}_7\text{Si}_{32}$  composition plotted in figure 8.2, we do not observe any distinct peaks of elements, but rather consistent small finite DOS around  $E_F$  in all elements. The sole composition with clear evidence of a spin down gap is from the chromium poor system plotted in figure 8.1 d. Also in this structure we see that the effects of Mn around  $E_F$  is dominant in spin down from the relative large amounts of Mn, but in comparison to the other composition these states are pushed away from the Fermi energy.

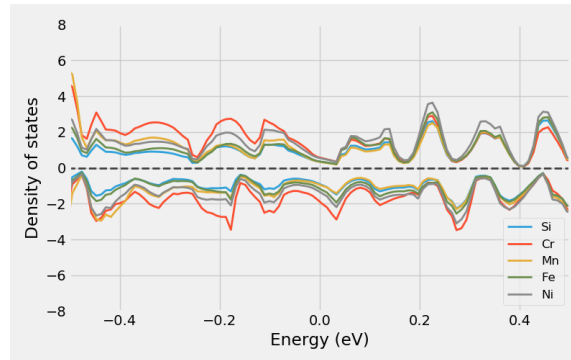


Figure 8.2: Projected density of states of  $\text{Cr}_3\text{Fe}_3\text{Mn}_3\text{Ni}_7\text{Si}_{32}$  around  $E_F$

An important factor of these results is that because each composition alters simultaneous elements, interpreting and relating the results to a particular alteration is challenging. For example, is the result of the  $\text{Cr}_5\text{Fe}_3\text{Mn}_5\text{Ni}_3\text{Si}_{32}$  permutation a consequence of less Fe or increments to both Cr and Mn? Furthermore is the large band gap in spin up of  $\text{Cr}_3\text{Fe}_3\text{Mn}_7\text{Ni}_3\text{Si}_{32}$  a product of increasing manganese or reducing the other elements. From the comparatively large gaps in spin up of  $\text{Cr}_3\text{Fe}_3\text{Mn}_7\text{Ni}_3\text{Si}_{32}$  and  $\text{Cr}_3\text{Fe}_5\text{Mn}_5\text{Ni}_3\text{Si}_{32}$  and the more present Cr states in spin up in the Cr rich permutations we here conclude that the band gap

is related to lessening of chromium, more so than other effects. However we see from both  $\text{Cr}_5\text{Fe}_5\text{Mn}_4\text{Ni}_3\text{Si}_{32}$  and  $\text{Cr}_3\text{Fe}_3\text{Mn}_3\text{Ni}_7\text{Si}_{32}$  (figure 8.2) in addition to the manganese rich composition that Mn plays a vital role on the band gap of these structures. It's clear that the  $\text{Cr}_3\text{Fe}_5\text{Mn}_5\text{Ni}_3\text{Si}_{32}$  alloy manage to strike a balance between 3d elements that results in a specific interplay and correspondingly very promising properties. It would have been beneficiary to look at for example the pair distribution functions and compare to the equimolar system, but from the factors discussed in section 7.2.4 we leave this to future work.

As stated before, we relied on the PBE GGA functional to determine the band gap in this part from its reliability and favorably computation cost. However we have conducted calculations with SCAN and HSE06 on some of the more promising structures. For instance in SQS D of  $\text{Cr}_3\text{Fe}_5\text{Mn}_5\text{Ni}_3\text{Si}_{32}$  we get lower values in both spin up and down with SCAN, specifically  $E_{G, \text{SCAN}}^{\text{up}} = 0.21$  eV and  $E_{G, \text{SCAN}}^{\text{dw}} = 0.08$  eV, and on the other hand HSE06 predicts  $E_{G, \text{HSE06}}^{\text{up}} = 0.53$  eV and  $E_{G, \text{HSE06}}^{\text{dw}} = 0$  eV. In SQS B of  $\text{Cr}_3\text{Fe}_3\text{Mn}_7\text{Ni}_3\text{Si}_{32}$  we observe very different outcomes. With SCAN we get a small band gap in spin down of about 0.002 eV and 0 in spin up, likewise the HSE06 band gap of this structure is  $E_{G, \text{HSE06}}^{\text{up}} = 0.08$  eV and  $E_{G, \text{HSE06}}^{\text{dw}} = 0.11$  eV, opposed to  $E_{G, \text{PBE}}^{\text{up}} = 0.47$  eV and  $E_{G, \text{PBE}}^{\text{dw}} = 0$  eV. Further the HSE06 band gap is in fact an impurity band gap, with  $E_{G, \text{HSE06}}^{\text{up, eigen}}(0.01) = 0.18$  eV and  $E_{G, \text{HSE06}}^{\text{dw, eigen}}(0.01) = 0.16$  eV.

## 8.2 High entropy silicides with cobalt/titanium

In similar fashion to the preceding section, we begin by presenting the new high-entropy silicides by the mean and standard deviation of the total energy and magnetization of 5 unique SQSs of each alloy in table 8.3. The compositions we have tested are deliberate combinations intended to investigate the role elements in the  $(\text{CrFeMnNi})\text{Si}_2$  system, by introducing Co/Ti at the cost of different elements. Note that the alloys contain a total of 48 atoms as before, based on the  $\beta$ - $\text{FeSi}_2$  unit cell and equimolar distribution of 3d elements.

Composition	Toten (eV)		Mag ( $\mu_B$ )		$E_{FPA}$ (eV)
	mean	std	mean	std	mean
$\text{Cr}_4\text{Fe}_4\text{Co}_4\text{Ni}_4\text{Si}_{32}$	- 6.466	0.006	0.008	0.016	-0.308
$\text{Co}_4\text{Fe}_4\text{Mn}_4\text{Ni}_4\text{Si}_{32}$	- 6.473	0.005	0.000	0.000	-0.355
$\text{Cr}_4\text{Fe}_4\text{Ti}_4\text{Ni}_4\text{Si}_{32}$	- 6.422	0.009	0.031	0.029	-0.209
$\text{Cr}_4\text{Fe}_4\text{Mn}_4\text{Ti}_4\text{Si}_{32}$	-6.699	0.007	0.114	0.064	-0.199
$\text{Cr}_4\text{Fe}_4\text{Mn}_4\text{Co}_4\text{Si}_{32}$	-6.769	0.003	0.133	0.033	-0.323

Table 8.3: Overview new compositions

In terms of the formation energy, we observe that cobalt evidently yield

the utmost stable alloys from the tested compositions, with (CoFeMnNi)Si<sub>2</sub> at the top and (CrFeCoNi)Si<sub>2</sub> at the bottom. On the other side, both (CrFeTiNi)Si<sub>2</sub> and (CrFeMnTi)Si<sub>2</sub> where we introduce titanium in place of manganese and nickel respectively, result in the overall least stable compositions. A precise physical interpretation of the stability between compositions is challenging from the shallow analysis in this project, but we do note that the two most stable alloys consist of the most chemically similar elements with respect to properties such as the electronegativity and atomic size. Following the least stable alloys are comprised of the most chemically dissimilar elements. This is in good agreement with the discussion in section 2.2 regarding phase formation of high-entropy alloys. Additionally, in the compositions discussed in the previous section we found that the most stable composition was Cr<sub>3</sub>Fe<sub>5</sub>Mn<sub>5</sub>Ni<sub>3</sub>Si<sub>32</sub> where the Cr proportion was lessened. In conjunction with the results of the titanium we thus may suspect that smaller elements are ill-suited in this structure.

In line with the other compositions studied in this project, the magnetization is clearly related to chromium and manganese also in this case. This is seen by the overall lowest magnetic moments in the two compositions without these elements, and reversely the highest magnetic moments is found for compositions with both Cr and Mn. Comparing the magnetic moment of (CrFeCoNi)Si<sub>2</sub> and (CoFeMnNi)Si<sub>2</sub> it seems in our study that chromium is most responsible for the magnetic moment in these alloys. Furthermore we find that substituting Ni with both Ti and Co yields more magnetic compounds. As we have discussed previously, the uniqueness of each SQS makes it difficult to draw conclusion on the various properties. In table 8.4 below we list the magnetic moment of the utmost stable SQS in each alloy. Contrary to the mean value we find that (CrFeCoNi)Si<sub>2</sub> equal to (CoFeMnNi)Si<sub>2</sub> is nonmagnetic, moreover (CrFeMnTi)Si<sub>2</sub> are less magnetic relative to both (CrFeMnCo)Si<sub>2</sub> and (CrFeMnNi)Si<sub>2</sub>.

Composition	Magnetic moment ( $\mu_B$ )
Cr <sub>4</sub> Fe <sub>4</sub> Co <sub>4</sub> Ni <sub>4</sub> Si <sub>32</sub>	0
Co <sub>4</sub> Fe <sub>4</sub> Mn <sub>4</sub> Ni <sub>4</sub> Si <sub>32</sub>	0
Cr <sub>4</sub> Fe <sub>4</sub> Ti <sub>4</sub> Ni <sub>4</sub> Si <sub>32</sub>	0,065
Cr <sub>4</sub> Fe <sub>4</sub> Mn <sub>4</sub> Ti <sub>4</sub> Si <sub>32</sub>	0,079
Cr <sub>4</sub> Fe <sub>4</sub> Mn <sub>4</sub> Co <sub>4</sub> Si <sub>32</sub>	0,167

Table 8.4: Final magnetic moment of the utmost stable SQS of each composition.

Thus, based on the utmost stable configurations we can state that replacing either Cr or Mn (with Co), removes the magnetic moment of the alloy. Furthermore we find that the magnetic moment is reduced when Ni is substituted with Ti, and increased by Co. However, while substituting manganese with Co yields a nonmagnetic alloy, Ti for Mn only slightly

reduces the magnetic moment.

In regards to the band gap, we find most to be metals. In table 8.5 we list the band gap of the utmost stable SQS of each composition, where the band gap is determined from the eigenvalues at different occupancy cutoff  $occ$  values to underline the effect of defect states. We find that increasing the criteria, in other words only consider states with occupancy above a certain threshold, the band gap become finite with  $occ = 0.1$  and converge to around  $0.02 - 0.06$  eV depending on composition at  $occ = 0.01$  and beyond.

Composition	$occ$	$E_G^{\text{up, eigen}}$ (eV)	$E_G^{\text{dw, eigen}}$ (eV)	$E_G^{\text{tot, eigen}}$ (eV)
CrFeCoNiSi <sub>2</sub>	0.5	0	0	0
	0.1	0.001	0.040	0.001
	0.01	0.063	0.063	0.063
CrFeTiNiSi <sub>2</sub>	0.5	0.007	0	0
	0.1	0.061	0.009	0.009
	0.01	0.061	0.037	0.037
CoFeMnNiSi <sub>2</sub>	0.5	0	0	0
	0.1	0.004	0.004	0.004
	0.01	0.027	0.027	0.027
CrFeMnTiSi <sub>2</sub>	0.5	0	0	0
	0.1	0.021	0.001	0
	0.01	0.030	0.030	0.022
CrFeMnCoSi <sub>2</sub>	0.5	0.461	0	0
	0.1	0.607	0.022	0.022
	0.01	0.607	0.025	0.025

Table 8.5: The band gap in spin up/down and total of the most stable SQS of high-entropy silicides based on  $\beta$ -FeSi<sub>2</sub> with cobalt/titanium.

The CrFeMnCoSi<sub>2</sub> composition exhibits a band gap of around 0.5 eV in spin up, contrary to the metallic compositions. We observe that the gap similar to the Cr<sub>5</sub>Fe<sub>5</sub>Mn<sub>3</sub>Ni<sub>3</sub>Si<sub>32</sub> composition and the the 192-atom SQS in section 7.2.5, is an impurity gap that contain a small number of defect states. As was the case in these structures, the band gap in (CrFeMnCo)Si<sub>2</sub> display small nonzero DOS at the Fermi energy, as seen from the projected density of states in figure 8.3. As observed in the previous compositions, the PDOS in this alloy point to a severe number of manganese states in spin down at energies just above  $E_F$ , and further large number of Cr states right below  $E_F$  in spin up.

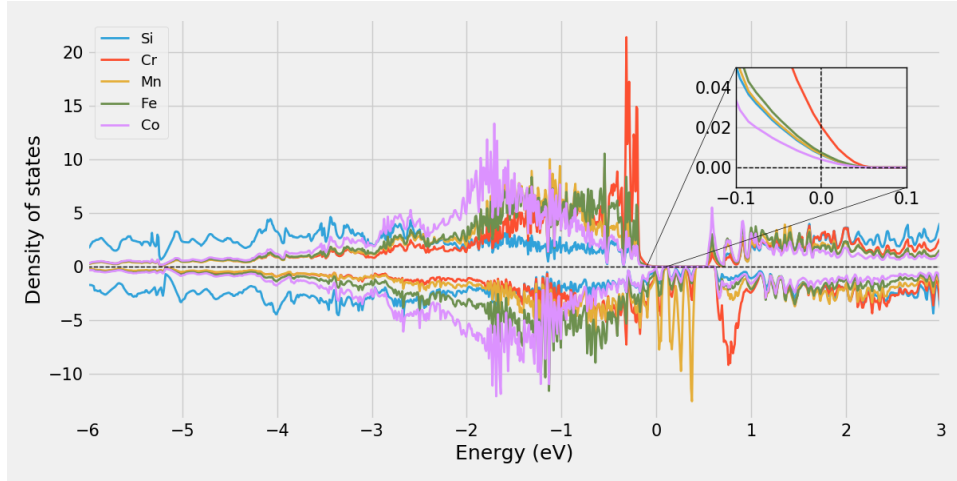


Figure 8.3: Projected density of states of  $(\text{CrFeMnCo})\text{Si}_2$ .

The PDOS of the other four alloys are displayed in figure 8.4 below. In agreement with the values listed in table 8.5 we observe clear indication of metallic structures, furthermore in agreement with the magnetic moments discussed previously.

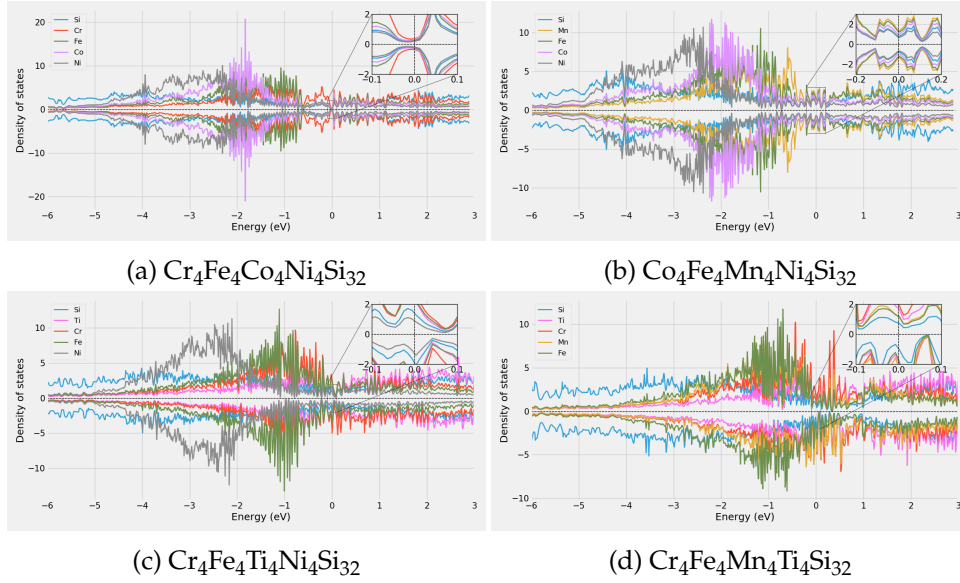


Figure 8.4: Projected density of states

Above we have evaluated the band gap of the different alloys based on the most stable configuration. Across all five configurations we find that the band gap is more or less consistent in  $(\text{CrFeCoNi})\text{Si}_2$ ,  $(\text{CrFeMnTiSi}_2)$ ,  $(\text{CrFeTiNi})\text{Si}_2$  and  $(\text{CrFeMnCo})\text{Si}_2$ . The most interesting case is the  $\text{CoFeMnNiSi}_2$  alloy, here we observed very narrow total band gaps in two lesser stable configurations (SQS A and E) of 0.03 eV and 0.006 eV respectively. The density of states of these structures are displayed in figure 8.5.



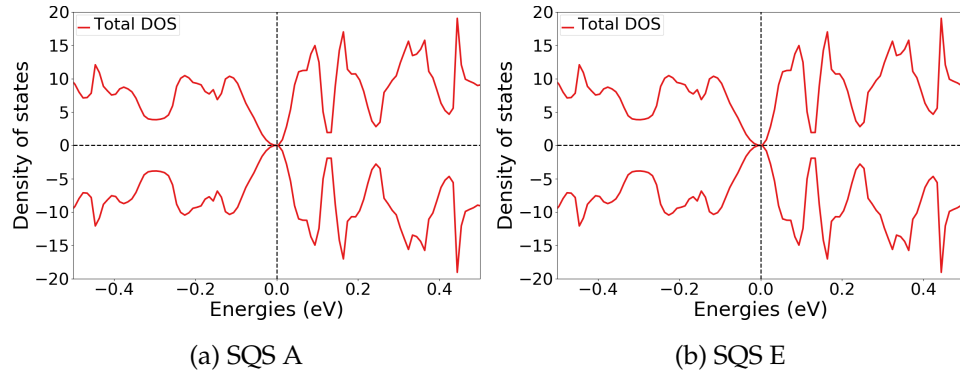


Figure 8.5: Density of states of SQS A and E of  $(\text{CoFeMnNi})\text{Si}_2$ .

### 8.3 Negative systems

In the above sections we have observed that aside from the  $(\text{CrFeMnNi})\text{Si}_2$  alloy, we experience limited success in locating semiconducting compounds, particularly when moving away from the  $\text{Cr:Fe:Mn:Ni:Si}$  system. In addition to compounds discussed above, we have performed simulations of computations of

In addition to the compounds discussed above, we attempted to replicate the  $\text{CrFeMnNi}$  system based on other silicides, such as hexagonal  $\text{CrSi}_2$ , trigonal  $\text{Fe}_2\text{Si}$ , and tetragonal and orthorhombic  $\text{Mn}_4\text{Si}_7$ , but found no indication of a band gap in these alloys. Furthermore we have tested a few alloys consisting of Sc, V, Zn, and Cu as well, but found no band gaps in these compositions either.

## **Part IV**

# **Conclusion and future work**

## Chapter 9

# Conclusion

High-entropy alloys has emerged as a rapidly growing interest in materials science from the large range of possibilities and flexibility. In this project we have set out to study the possibility of a narrow gap semiconducting high-entropy silicide with top of the line computational power and methods, in the prospect of discovering next-generation efficient thermoelectric materials. The materials in mind were based on the  $\text{FeSi}_2$  semiconductor, and modeled with the SQS method in the framework of DFT. To study the potential semiconductors we generated five distinct configurations of each composition and investigated the band gap, mainly with PBE GGA.

Our most successful effort was based around a 48-atom model of chromium, iron, manganese, and nickel in the  $\text{Cr:Fe:Mn:Ni:Si}$  system. In the equimolar composition  $(\text{CrFeMnNi})\text{Si}_2$ , we observed large variation of the band gap between the five distinct configurations. In spin up, the band gap ranged from 0.08 - 0.34 eV. The most stable supercell was a half-metal, while the other four supercells displayed small spin down gaps between 0.03 eV and 0.05 eV as well. Calculations with SCAN and HSE06 produced unpredictable outputs that varied greatly between SQSs, and contained a larger degree of uncertainty compared to PBE. However, with HSE06 we found spin up band gaps of 0.55 eV and 0.71 eV in two respective supercells, and a total band gap of 0.18 eV in another. Contrary, the SCAN functional resulted in total band gaps around 0.1 in three SQSs, one metallic supercell and one half-metallic structure with a spin down band gap of 0.1 eV.

Following the equimolar composition, we conducted a brief exploration of the quasi-ternary phase diagram of this composition. Contrary to the equimolar system we found here more frequently half-metals. By analyzing the projected density of states we were able to relate the metallic spin down channel to a dominant presence of manganese states around the Fermi energy. Inside the compositions that we tested, we found evidence for that there exists a positive relation between the band gap in this system, most notably in spin up, and compositions poor in chromium and/or rich in manganese. Specifically, we found two very positive compositions:  $\text{Cr}_3\text{Fe}_3\text{Mn}_7\text{Ni}_3\text{Si}_{32}$  and  $\text{Cr}_3\text{Fe}_5\text{Mn}_5\text{Ni}_3\text{Si}_{32}$ , where the most stable supercell of the former displayed a spin up band gap of 0.47 eV, and the latter a total

band gap of 0.1 eV, with PBE.

Lastly, we tested various compositions where we introduced cobalt/titanium at the cost of either Cr, Mn or Ni. Based on the most stable configuration in each of these compositions, the only band gap we found in this experiment was a spin up band gap of 0.46 eV in  $(\text{CrFeMnCo})\text{Si}_2$ . By manually investigating the calculated eigenvalues of the different compositions, we were able to relate the metallic compounds to defect states in the band gap. This is a familiar term in random alloys, in which states at the band edges deviate slightly from completely full/empty occupancy. The effect and occurrence of defect states varied from composition to composition and supercell to supercell, for instance in the Cr:Fe:Mn:Ni:Si system, defects states was most prominent for spin down states, which resulted in several half-metallic structures.

In accordance with the spin polarization of the band gap, we noted a finite magnetic moment in most alloys. Distinctly, the equimolar alloy contained a magnetic moment of  $0.083\mu_B$  in all five configurations of the equimolar alloy. Upon investigation of the local magnetic moments, we discovered that the magnetism was mainly attributed to chromium and manganese atoms in the lattice. This was found as a general trend for all alloys based on the  $\text{FeSi}_2$  structure. Due to this severe spin polarization, a possible application of these alloys, particularly the Cr:Fe:Mn:Ni:Si alloys, could be as spintronics [10].

In terms of thermoelectric application, we find limited success in respect to the band gap. Recalling that good thermoelectrics are semiconductors with band gaps around 0.2 eV, we observe that the semiconducting band gaps of the  $(\text{CrFeMnNi})\text{Si}_2$  are too small. However, we have found instances more suitable, such as the HSE06 band gap of 0.18 eV in one of the supercells. Furthermore, we can expect that the band gaps in the real material are larger than the PBE band gaps, thus there is a possibility that the  $(\text{CrFeMnNi})\text{Si}_2$  alloy could be applied as a thermoelectric. Nevertheless, to qualitatively state the thermoelectric applicability of this compound, we would have to study properties such as the Seebeck coefficient, as well the thermal and electrical conductivity.

## Chapter 10

### Future work

In future studies on this system, I would first and foremost try to resolve several of the uncertainties circling the results presented in this project. This would include a more thoughtful investigation of the true ground state of the  $(\text{CrFeMnNi})\text{Si}_2$  composition, by first testing multiple configurations and a larger number of SQS sizes to reduce variance and obtain a converged value of the band gap. Secondly, to decide on the most representative configuration we should have put more efforts into correctly/optimally specify the magnetic configuration of each SQS, and study excited states of the alloys to account for entropic contributions to the stability. Moreover, a test of different crystal structures in addition to the orthorhombic CMCE space group of the  $(\text{CrFeMnNi})\text{Si}_2$  alloy should be done, as the local minima method of DFT does not guarantee that this is the most stable conformation of the alloy.

The overarching motivation of this thesis have been to simply locate a band gap in high-entropy silicides, which by no means have been simple. However, now that we have located such a compound, in future work we would like to devote more effort into specifically analyze the band gap. Potentially try to plot and analyze the band structure of the alloy and qualitatively study the band gap by different functionals. Furthermore, we performed only a very limited search of the quasi-ternary phase diagram of the Cr:Fe:Mn:Ni:Si system, but found promising results in the direction of less chromium and more in manganese. Thus, a future study of more deliberate compositions in these directions would also be interesting. Provided that these results yielded positive outcomes of the band gap, suitable for thermoelectric application, future work could focus on a complete study of this material as a thermoelectric, and consider factors such as the Seebeck coefficient and electrical and thermal conductivity.

# Bibliography

- [1] termoelektrisitet. *Velkommen til en termoelektrisk verden!* nor. Nov. 2013. URL: <https://termoelektrisitet.no/2013/11/24/velkommen-til-en-termoelektrisk-verden/> (visited on 24/11/2013).
- [2] Wikipedia. *Thermoelectric materials*. en. Page Version ID: 989933448. Nov. 2020. URL: [https://en.wikipedia.org/w/index.php?title=Thermoelectric\\_materials&oldid=989933448](https://en.wikipedia.org/w/index.php?title=Thermoelectric_materials&oldid=989933448) (visited on 22/11/2020).
- [3] Eddwi H. Hasdeo et al. 'Optimal band gap for improved thermoelectric performance of two-dimensional Dirac materials'. In: *Journal of Applied Physics* 126.3 (July 2019), p. 035109. ISSN: 1089-7550. DOI: 10.1063/1.5100985. URL: <http://dx.doi.org/10.1063/1.5100985>.
- [4] G. Jeffrey Snyder and Eric S Toberer. 'Complex thermoelectric materials'. eng. In: *Nature materials* 7.2 (2008), pp. 105–114. ISSN: 1476-1122.
- [5] Jorge Osvaldo Sofo and GD Mahan. 'Optimum band gap of a thermoelectric material'. In: *Physical Review B* 49.7 (1994), p. 4565.
- [6] Tsai. Ming-Hung and Yeh. Jien-Wei. 'High-Entropy Alloys: A Critical Review'. In: *Materials Research Letters* 2.3 (2014), pp. 107–123. DOI: 10.1080/21663831.2014.912690. eprint: <https://doi.org/10.1080/21663831.2014.912690>. URL: <https://doi.org/10.1080/21663831.2014.912690>.
- [7] Joshua Gild et al. 'A high-entropy silicide: (Mo<sub>0.2</sub>Nb<sub>0.2</sub>Ta<sub>0.2</sub>Ti<sub>0.2</sub>W<sub>0.2</sub>)Si<sub>2</sub>'. In: *Journal of Materiomics* 5.3 (2019), pp. 337–343. ISSN: 2352-8478. DOI: <https://doi.org/10.1016/j.jmat.2019.03.002>. URL: <https://www.sciencedirect.com/science/article/pii/S2352847819300334>.
- [8] Mari Mathillas Røsvik. *Structural Characterization of High Entropy Metal Silicide Alloys*. 2021.
- [9] Burkov. A. 'Silicide Thermoelectrics: Materials for Energy Harvesting'. In: *physica status solidi (a)* 215 (June 2018). DOI: 10.1002/pssa.201800105.
- [10] Xingxing Li and Jinlong Yang. 'First-principles design of spintronics materials'. In: *National Science Review* 3.3 (Apr. 2016), pp. 365–381. ISSN: 2095-5138. DOI: 10.1093/nsr/nww026. eprint: <https://academic.oup.com/nsr/article-pdf/3/3/365/31566317/nww026.pdf>. URL: <https://doi.org/10.1093/nsr/nww026>.